The Astrophysical Journal, 694:546–555, 2009 March 20 doi:10.1088/0004-637X/694/1/546
© 2009. The American Astronomical Society. All rights reserved. Printed in the U.S.A.

IR DUST BUBBLES. II. PROBING THE DETAILED STRUCTURE AND YOUNG MASSIVE STELLAR POPULATIONS OF GALACTIC H II REGIONS

C. Watson[1], T. Corn[1], E. B. Churchwell[2], B. L. Babler[2], M. S. Povich[2], M. R. Meade[2], and B. A. Whitney[3]
[1] Manchester College, Department of Physics, 604 E. College Avenue, North Manchester, IN 46962, USA
[2] Department of Astronomy, University of Wisconsin–Madison, 475 N. Charter St., Madison, WI 53716, USA
[3] Space Science Institute, 4750 Walnut St. Suite 205, Boulder, CO 80301, USA
Received 2008 August 25; accepted 2008 December 23; published 2009 March 17

ABSTRACT

We present an analysis of late-O/early-B-powered, parsec-sized bubbles and associated star formation using Two Micron All Sky Survey, GLIMPSE, MIPSGAL, and MAGPIS surveys. Three bubbles were selected from the Churchwell et al. catalog. We confirm that the structure identified in Watson et al. holds in less energetic bubbles, i.e., a photodissociated region, identified by 8 μm emission due to polycyclic aromatic hydrocarbons surrounding hot dust, identified by 24 μm emission and ionized gas, and identified by 20 cm continuum. We estimate the dynamical age of two bubbles by comparing bubble sizes to numerical models of Hosokawa and Inutsuka. We also identify and analyze candidate young stellar objects using spectral energy distribution (SED) fitting and identify sites of possible triggered star formation. Lastly, we identify likely ionizing sources for two sources based on SED fitting.

Key words: H II regions – infrared: stars – stars: formation

Online-only material: color figures

1. INTRODUCTION

Massive stars strongly influence their surrounding environment throughout their lifetime via stellar winds, ionizing radiation, heating of dust, and expansion of their H II regions. Some of these processes may trigger second-generation star formation by compressing neighboring pre-existing molecular material to the point of gravitational instability. Observing massive star formation regions, however, has been hampered by large UV and optical extinction. These regions are observed at IR, radio, and X-ray wavelengths where extinction is significantly smaller.

Churchwell et al. (2006, 2007) analyzed mid-IR (MIR) images from the *Spitzer*-GLIMPSE project, a survey of the Galactic plane ($|b| < 1°$, $|l| < 65°$; Benjamin et al. 2003), and found bubbles of diffuse emission to be a signature structure in the interstellar medium (ISM) at MIR wavelengths. They cataloged almost 600 bubbles (an admittedly incomplete catalog) in the GLIMPSE survey area. They argued based on the location and coincidence with known H II regions that many of the MIR bubbles are produced by O and early-B stars. Watson et al. (2008) analyzed the structure of three bubbles and associated star formation using surveys in the MIR (GLIMPSE and MIPSGAL) and radio continuum (MAGPIS). They concluded that the general structure of the bubbles is a photodissociated region (PDR), visible in the 5.8 and 8 μm Infrared Array Camera (IRAC) bands on *Spitzer*, which encloses ionized gas (observed at 20 cm) and hot dust (observed at 24 μm). One bubble (N49) showed evidence of a cavity at 24 μm and 20 cm, indicating that hot dust and ionized gas have been evacuated by stellar winds. They also characterized the young stellar objects (YSOs) associated with each bubble and identified sites of probable triggered star formation and sources likely responsible for ionizing hydrogen and exciting the PDR.

Deharveng and collaborators have studied PDRs and triggered star formation around the H II regions Sh 217 and Sh 219 (Deharveng et al. 2003a), Sh 104 (Deharveng et al. 2003b), RCW 79 (Zavagno et al. 2006), SH2-219 (Zavagno et al. 2006), and RCW 120 (Zavagno et al. 2007). They identified several sites of probable triggered star formation, some by the collapse of pre-existing clouds (observed at 1.2 mm continuum) and some by the collect-and-collapse mechanism (see Whitworth et al. 1994; Elmegreen 1998, and references therein). Briefly, the collect-and-collapse mechanism posits that ambient ISM is swept-up by an expanding H II region, increasing in density until one or more subcomponents become gravitationally unstable and collapse, leading to star formation. For some of these regions, they estimated ages for the H II region and masses for the surrounding millimeter clumps. They also classified the YSOs in the regions into the standard classes based on near and MIR colors.

Here, we analyze the gas and dust structure in three GLIMPSE-identified bubbles in the Churchwell et al. (2007) catalog. We also measure star formation activity and identify YSOs to characterize possible triggering mechanisms. Three sources were chosen for their range of sizes, association with likely triggered star formation, bubble dynamical ages, and spectral types of the ionizing star(s). All are at low longitudes ($|l| < 10°$). In Section 2, we introduce each source and the surveys used. In Section 3, we discuss the relative position of gas and dust components (polycyclic aromatic hydrocarbons (PAHs), ionized gas, and dust), identify YSOs and analyze their properties and identify candidate ionizing stars in each bubble. In Section 4, we discuss the results in the context of triggered star formation mechanisms. Our main conclusions are summarized in Section 5.

2. DATA

Data were collected from four large-scale surveys: Two Micron All Sky Survey (2MASS), GLIMPSE, MIPSGAL, and MAGPIS. The 2MASS All-Sky Point-Source Catalog covers over 99% of the sky at bands J, H, and K_s. Along with the mosaiced images from GLIMPSE, we used the GLIMPSE Point-Source Catalog (GPSC), a 99.5% reliable catalog of point sources observed in the *Spitzer*-IRAC bands (3.6, 4.5, 5.8, and 8.0 μm). IRAC has a resolution of 1.″5–1.″9 (3.6–8.0 μm). See the

GLIMPSE Data Products Description[4] for details. MIPSGAL is a survey of the same region as GLIMPSE, using the MIPS instrument (24 μm and 70 μm) on *Spitzer*. MIPSGAL has a resolution of 6″ at 24 μm and 18″ at 70 μm. MAGPIS is a survey of the Galactic plane at 20 cm and 6 cm using the VLA in configurations B, C, and D combined with the Effelsburg 100 m single-dish telescope (White et al. 2005). MAGPIS has a resolution of 6″ at both wavelengths.

We analyze CN138, CN108, and CS57 from the Churchwell et al. (2007) catalog of bubbles. All sources are within 10° of the Galactic center and have not been studied in detail previously. CN138 is near *IRAS* source 18073−2046, which has been studied by Mateen et al. (2006) in SO $J = 1$–0, Scoville et al. (1987) in radio recombination lines, Walsh et al. (1997) in methanol masers, and by Slysh et al. (1999) in methanol masers. However, IRAS 18073−2046 appears to be coincident with CN139 in the bubble catalog, a large, complex bubble. Here, we choose to isolate our analysis to the morphologically simpler and smaller CN138, which has not been studied previously. There are two *IRAS* sources present toward CN108: IRAS 18028−2208 and IRAS 18029−2213. A Wolf–Rayet (W–R) star was identified by Shara et al. (1999) at $l = 8\overset{\circ}{.}02$, $b = -0\overset{\circ}{.}42$ on the boundary of CN108 in projection. CN108 was also observed by Lockman et al. (1996) in the radio recombination lines H109α and H111α with the Green Bank 140 ft telescope. Near CS57, IRAS 17262−3435 is observed in the PDR shell and IRAS 17258−3432 is observed outside the PDR shell. No other known observations of these bubbles exist besides the surveys summarized above. Velocity measurements are available for all the bubbles and are summarized in Section 3.

3. RESULTS

All three sources show the same basic structure of gas and dust that Watson et al. (2008) observed in three other bubbles: a PDR shell (identified by 5.8 μm and 8 μm PAH emission) surrounding hot dust (identified by 24 μm emission). In two sources (CN138 and CN108), the PDR also surrounds ionized gas (identified by radio continuum emission that overlaps with the 24 μm emission). We now present the MIR observations, YSO properties and ionizing star candidates for the three selected sources (CN138, CN108, and CS57).

3.1. CN138

CN138 has a shell morphology at 8 μm that surrounds 24 μm and 20 cm emission (see Figure 1). Its kinematic distance is 4.3 ± 0.6 kpc (based on a radio recombination line velocity of 34 km s^{-1}, see Scoville et al. 1987, and the rotation model of Brand & Blitz 1993). Errors are calculated assuming departures from circular velocities of 10 km s^{-1}. We measure the average radius to the inner boundary of the 8 μm shell to be ∼80″ (∼1.7 pc), the FWHM of the 24 μm emission to be ∼54″ (∼1.1 pc), and the FWHM at 20 cm emission to be 36″ (0.8 pc). The 24 μm and 20 cm difference in radii may be due to the low sensitivity of the 20 cm observations. As shown in Figure 1 (bottom), the 20 cm and 24 μm emission peaks significantly overlap, while the 8 μm emission peaks are offset and surround the 20 cm and 24 μm emission peaks. The integrated flux density at 20 cm is 0.19 Jy, indicating an ionizing flux of $N_{\rm Ly} = 2.9 \times 10^{47}$ photons s^{-1}, equivalent to a B0–B0.5 star (based on extrapolating Martins et al. 2005, hereafter MSH05, to B-type stars).

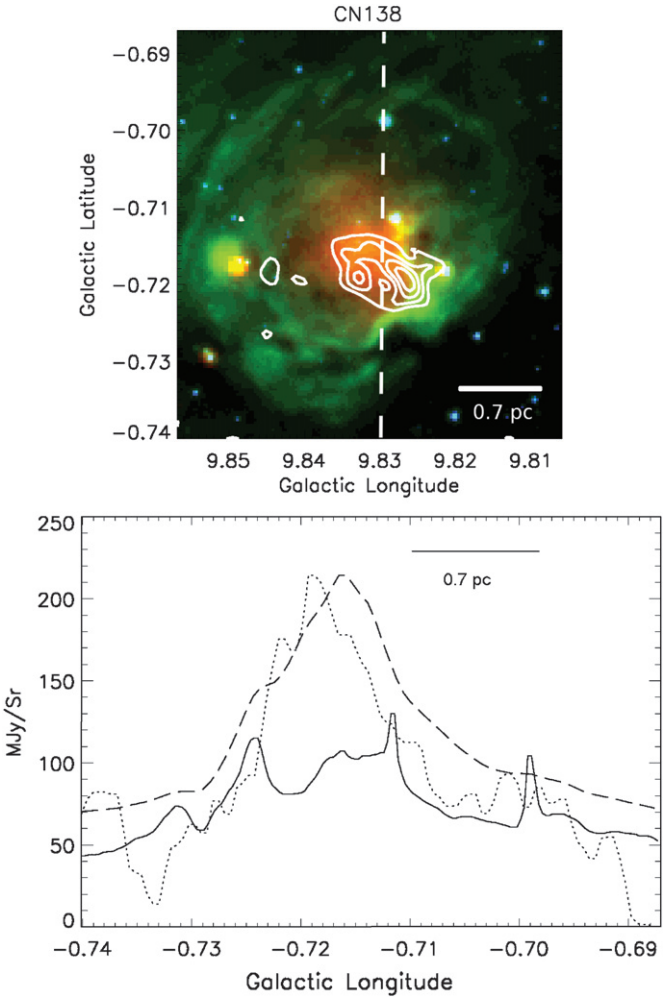

Figure 1. Top: CN138 shown in 24 μm (red), 8 μm (green), and 4.5 μm (blue). 20 cm in contours at 1.5, 1.8, 2.1, and 2.4 mJy beam^{-1}. The distance indicated at the lower right is calculated using a kinematic distance of 4.3 kpc. Bottom: slice at $l = 9\overset{\circ}{.}83$. 20 cm (dotted, $\times 10^6$), 24 μm (dashed), and 8.0 μm (solid, $\times 5$). The 20 cm and 24 μm are largely contained within the 8 μm peaks which represent the shell.

(A color version of this figure is available in the online journal.)

There are 1850 sources in the GPSC within 300″ (6.7 pc) of the center of CN138. We chose a relatively large area surrounding CN138 to show the star formation associated with CN139. We performed point-source photometry on the MIPSGAL images and cross-correlated the resultant 24 μm sources with the corresponding GPSC sources. These sources were then analyzed using the YSO-fitting method of Robitaille et al. (2007). Briefly, this method involves a grid of Monte Carlo radiative transfer models of YSOs with specified stellar masses, luminosities, disk masses, mass accretion rates, and line-of-sight (LOS) inclinations (Robitaille et al. 2006). Observations from the J-band to 24 μm are fitted using a χ^2-minimization technique. The range of models that fit the observations within the observational errors gives an implied range of YSO physical properties. All the YSOs surrounding CN138 are shown in Figure 2, and the range of stellar masses, total luminosities, and envelope accretion rates are given in Table 1. The large area in Figure 2 is shown to demonstrate CN139 (to the lower left) and the star formation that is not associated with the shell of CN138 (see below). Each YSO is classified as stage 0 if $\dot{M}_{\rm env}/M_* > 10^{-6}$ yr^{-1}, stage I if $\dot{M}_{\rm env}/M_* < 10^{-6}$ yr^{-1} and

[4] http://www.astro.wisc.edu/glimpse/glimpse1_dataprod_v2.0.pdf

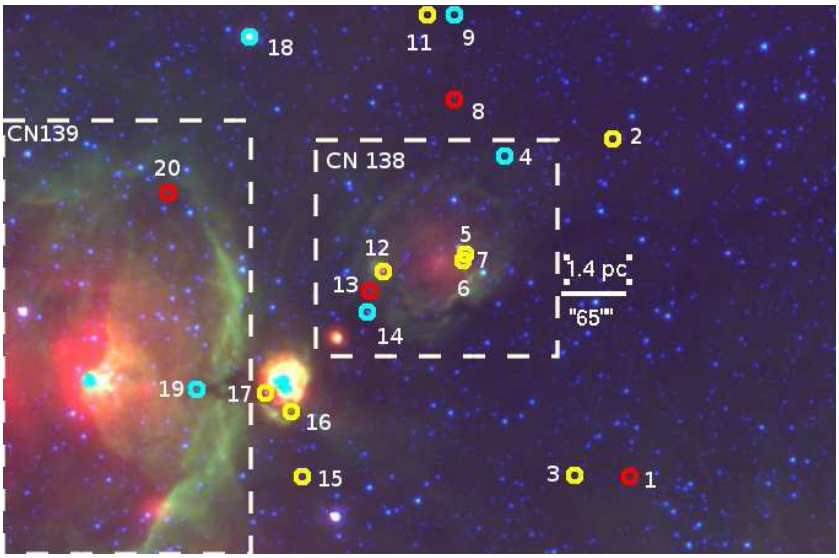

Figure 2. CN138: candidate YSOs identified using the numerical models and SED fitting explained in Robitaille et al. (2007) overlaid on 24 μm (red), 8.0 μm (green), and 4.5 μm (blue) images. Stage I sources are shown in yellow, stage II in cyan, and stage III in red. Two sites of possible triggered star formation are visible to the left and right of the bubble center. CN139, a nearby and larger bubble, is present to the left of CN138.

(A color version of this figure is available in the online journal.)

$\dot{M}_{\rm disk}/M_* > 10^{-6}$ yr^{-1}, or stage III if $\dot{M}_{\rm disk}/M_* < 10^{-6}$ yr^{-1} and $\dot{M}_{\rm env}/M_* < 10^{-6}$ yr^{-1}, following Robitaille et al. (2006).

Some of these candidate YSOs are likely foreground or background YSOs unassociated with the bubble as Povich et al. (2008) found toward the M17 complex. By analyzing an off-source control sample using the SKY model of IR point sources, they concluded that a majority of the contaminates were YSOs at unknown distances. We expect that the contamination of our sample with foreground or background sources would be higher at low galactic longitudes, since the LOS covers more volume than the earlier analysis. For these sources, the properties given in Table 1 are incorrect.

There are two sites of possible triggered star formation along the shell of CN138, to the right and left of the bubble center. Both groups of YSOs are low-to-intermediate mass ($M_* < 10\ M_\odot$). The lack of YSOs and dimmer 8 μm PAH emission along the rest of the rim implies that the density of the gas may be higher to the east and west (assuming roughly equal illumination by the hot star(s) that ionize CN138). This source is qualitatively similar to the rim surrounding RCW 79 (Zavagno et al. 2006). In their study of molecular gas and GLIMPSE data observed toward RCW 79, Zavagno et al. (2006) pointed out that the YSOs along the edge of the H II region formed distinct groups. One prediction of the collect-and-collapse model is that YSOs will form in such groups along the shock front of the expanding H II region. The groups are related to the gravitational instability length scale, modified by effects due to the expanding shock wave, pressure external to the shock wave, and the shock layer thickness. Zavagno et al. (2006) concluded that this mechanism was operative in RCW 79. In CN138, it also appears that the YSOs are formed into two distinct groups.

GPSC+MIPSGAL sources have been analyzed to find the ionizing star(s) responsible for CN138 following the process outlined in Watson et al. (2008). Since we lack spectra of these stars, this method was developed to identify candidate ionizing sources. Briefly, we identify those sources whose spectral energy distributions (SEDs) are consistent with an early-B or O-type star at the distance of the CN138 bubble with the following constraints: the source must be fit by a hot stellar photosphere model with no circumstellar emission, at the distance of the bubble (4.3 kpc, see above), there must be some extinction, and the source must lie inside projected bubble boundaries. Two sources were found consistent with the above criteria. Their locations are shown in Figure 3 and properties are given in Table 2. These sources are two subclasses earlier than implied by the radio continuum emission. One of these sources may be the ionizing star but the other is likely a foreground, cooler star. The discrepancy between the estimated spectral type of the ionizing star from the observed radio continuum is probably primarily due to dust absorption of UV photons in the H II region, which are not counted by radio continuum emission. There are, of course, uncertainties in determining spectral types using this method as well. Both of these possible ionizing stars are significantly off-center in projection with respect to the bubble. Since the bubble is not circular, however, it may be reasonable for the ionizing source to not be perfectly centered. However, the 24 μm emission peak is significantly offset from the candidate ionizing stars. These offsets may indicate that we have not identified the ionizing source for this bubble.

3.2. CN108

CN108 has a shell morphology at 8 μm that surrounds a smaller shell of 24 μm and 20 cm emission (see Figure 4). Its kinematic distance is 4.9 kpc (based on a radio recombination line velocity measurement of 37 km s^{-1} by Lockman et al. 1996). We measure the average inner radius of the 8 μm shell to be 340″ (8.0 pc) and the average outer radius to be 520″ (12 pc). The integrated 20 cm flux density is 13.6 Jy, equivalent to an ionizing flux of 1.9×10^{48} photons s^{-1} or a single O8V star (MSH05). The radio continuum, however, appears strongly over-resolved and this flux density is likely an underestimate.

All stars shown in Figure 5 have been analyzed using the model fitter of Robitaille et al. (2007) to identify candidate ionizing stars and YSOs associated with CN108. The locations of candidate YSOs are shown in Figure 5 and the properties are

Table 1
Model Parameters for Candidate YSOs

		$M_\star$ ($M_\odot$)		$L_{\rm TOT}$ ($L_\odot$)		$\dot{M}_{\rm env}$ ($M_\odot$ yr^{-1})		
ID	Name (G*l*+*b*)	Min	Max	Min	Max	Min	Max	Stage
CN138-1	G9.7813-0.7732	0.7	4.2	5	337	0	6.13E−6	III
CN138-2	G9.7861-0.6814	0.1	18.4	2	13880	0	3.06E−3	I
CN138-3	G9.7965-0.7729	0.3	7.1	3	932	0	6.18E−4	I
CN138-4	G9.8154-0.6861	0.2	6.2	2	1019	0	2.35E−4	II
CN138-5	G9.8261-0.7127	0.3	6.3	5	1100	0	5.38E−4	I
CN138-6	G9.8265-0.7172	3.6	14.5	140	7305	2.25E−5	1.88E−3	...
CN138-7	G9.8268-0.7143	0.7	10.5	8	2306	0	2.10E−3	I
CN138-8	G9.8291-0.6707	1.8	4.4	28	127	1.03E−8	5.63E−5	III
CN138-9	G9.8292-0.6478	0.5	5.0	2	469	0	1.88E−5	II
CN138-10	G9.8350-0.6358	5.3	10.9	544	8256	0	1.32E−3	II
CN138-11	G9.8366-0.6479	7.9	7.9	745	745	1.56E−4	1.56E−4	I
CN138-12	G9.8486-0.7176	1.0	6.5	24	331	4.18E−7	1.44E−3	I
CN138-13	G9.8523-0.7226	2.7	7.3	49	1942	0	0	III
CN138-14	G9.8529-0.7285	0.2	7.3	9	1995	0	9.36E−4	II
CN138-15	G9.8705-0.7731	0.4	5.4	5	321	0	6.18E−4	I
CN138-16	G9.8736-0.7553	1.6	22.5	48	61250	1.35E−5	4.68E−3	I
CN138-17	G9.8803-0.7506	0.2	20.0	13	35300	0	1.86E−3	I
CN138-18	G9.8849-0.6539	9.3	19.2	5882	41650	0	0	II
CN138-19	G9.8991-0.7493	0.2	13.4	9	7831	0	2.33E−3	II
CN138-20	G9.9067-0.6962	0.4	7.0	5	583	0	6.18E−4	III
CN108-1	G7.9828-0.4212	0.3	4.0	2	249	0	1.22E−4	II
CN108-2	G7.9954-0.5735	0.6	3.9	4	249	0	3.43E−5	II
CN108-3	G7.9960-0.5638	0.6	4.5	4	334	0	2.35E−4	II
CN108-4	G7.9980-0.5471	0.6	5.6	28	697	0	1.63E−3	I
CN108-5	G7.9985-0.5252	0.3	8.4	2	1159	0	1.78E−3	I
CN108-6	G8.0115-0.5845	0.4	4.1	3	234	0	1.47E−4	I
CN108-7	G8.0219-0.3233	0.4	10.6	11	2080	0	1.06E−3	I
CN108-8	G8.0243-0.5117	0.2	8.8	1	1159	0	2.81E−3	II
CN108-9	G8.0416-0.5169	0.2	4.6	2	361	0	1.80E−4	I
CN108-10	G8.0428-0.5472	0.4	4.1	3	249	0	8.85E−5	II
CN108-11	G8.0430-0.4532	0.3	4.1	2	249	0	1.80E−4	III
CN108-12	G8.0483-0.3122	0.8	5.1	6	487	0	2.35E−4	II
CN108-13	G8.0612-0.6618	3.9	4.0	52	53	3.43E−7	3.66E−7	II
CN108-14	G8.0620-0.3586	3.7	11.6	208	9883	0	0	III
CN108-15	G8.0625-0.4334	1.1	5.1	13	100	2.31E−7	2.40E−4	I
CN108-16	G8.0642-0.3804	2.3	3.5	28	121	0	0	III
CN108-17	G8.0653-0.5617	4.8	8.7	187	1217	2.53E−5	2.37E−3	I
CN108-18	G8.0686-0.3466	0.7	3.5	4	119	0	5.04E−7	III
CN108-19	G8.0725-0.4408	0.1	7.9	2	2734	0	5.41E−4	I
CN108-20	G8.0823-0.3555	0.5	5.0	4	469	0	1.22E−4	II
CN108-21	G8.0845-0.4357	2.3	3.5	28	121	0	0	III
CN108-22	G8.0908-0.4606	0.2	4.6	1	361	0	2.37E−4	III
CN108-23	G8.0911-0.5492	8.0	16.2	2714	17220	0	6.90E−3	I
CN108-24	G8.0924-0.5646	0.4	4.5	5	283	0	4.37E−4	III
CN108-25	G8.1012-0.2742	2.9	11.8	94	10220	0	1.07E−3	I
CN108-26	G8.1014-0.4731	2.3	10.7	81	4922	0	7.44E−4	I
CN108-27	G8.1040-0.4732	0.7	7.6	12	602	6.94E−9	4.69E−4	I
CN108-28	G8.1042-0.6382	0.6	3.9	7	55	1.93E−9	1.71E−4	II
CN108-29	G8.1063-0.5533	2.0	4.5	19	323	0	0	II
CN108-30	G8.1066-0.4568	0.2	8.5	9	3554	0	9.24E−4	I
CN108-31	G8.1076-0.4037	0.6	4.4	6	148	0	4.13E−5	II
CN108-32	G8.1085-0.3852	0.9	5.1	7	499	0	1.01E−4	II
CN108-33	G8.1110-0.2798	2.0	4.4	38	127	1.88E−6	1.97E−4	I
CN108-34	G8.1129-0.3593	0.4	8.8	2	1211	0	2.15E−3	I
CN108-35	G8.1129-0.3610	1.4	9.6	44	5151	0	2.33E−3	I
CN108-36	G8.1143-0.3268	0.7	6.2	8	1543	0	2.04E−4	II
CN108-37	G8.1161-0.3783	0.6	5.1	7	250	0	4.37E−4	I
CN108-38	G8.1161-0.6525	0.5	3.9	3	249	0	1.33E−4	II
CN108-39	G8.1176-0.2717	1.0	5.2	12	383	0	2.18E−4	II
CN108-40	G8.1184-0.2634	0.6	5.5	4	469	0	4.24E−5	II
CN108-41	G8.1201-0.4529	1.1	7.5	27	1690	3.98E−6	1.79E−3	I
CN108-42	G8.1203-0.4539	1.6	7.5	38	1017	1.20E−5	1.79E−3	I

Table 1
(Continued)

ID	Name (G*l*+*b*)	$M_\star$ ($M_\odot$)		$L_{\rm TOT}$ ($L_\odot$)		$\dot{M}_{\rm env}$ ($M_\odot$ yr^{-1})		Stage
		Min	Max	Min	Max	Min	Max	
CN108-43	G8.1365-0.2664	0.7	8.0	11	1224	0	1.79E−3	I
CN108-44	G8.1468-0.3420	0.2	4.6	1	361	0	2.50E−4	I
CN108-45	G8.1483-0.6319	0.5	4.2	3	249	0	4.13E−5	I
CN108-46	G8.1522-0.5630	0.3	4.0	2	213	0	8.85E−5	I
CN108-47	G8.1609-0.6646	4.6	8.4	383	3447	0	0	II
CN108-48	G8.1634-0.5083	11.3	23.7	9714	70880	0	0	II
CN108-49	G8.1667-0.5062	0.7	7.8	10	631	8.82E−8	9.41E−4	I
CN108-50	G8.1684-0.4060	0.5	4.6	4	361	0	1.71E−4	II
CN108-51	G8.1716-0.6643	0.5	3.8	4	178	0	1.22E−4	II
CN108-52	G8.1774-0.4662	0.4	8.7	5	1217	0	2.37E−3	I
CN108-53	G8.1832-0.2707	0.4	4.6	4	361	0	2.50E−4	I
CN108-54	G8.1903-0.5817	0.5	4.2	3	337	0	7.78E−5	II
CN108-55	G8.1906-0.3702	0.2	7.5	4	2150	0	4.67E−4	II
CN108-56	G8.1973-0.4937	0.5	4.2	5	161	0	1.02E−4	II
CN108-57	G8.2000-0.6423	2.0	7.5	40	510	3.31E−6	6.73E−4	I
CN108-58	G8.2003-0.3751	1.5	4.7	19	144	0	1.37E−4	I
CN108-59	G8.2010-0.2917	0.9	6.8	32	464	8.10E−8	8.65E−4	I
CN108-60	G8.2066-0.3452	2.1	8.0	40	1017	1.20E−5	1.79E−3	I
CN108-61	G8.2067-0.5951	0.4	4.6	2	361	0	6.65E−5	II
CN108-62	G8.2070-0.5448	0.2	4.3	1	261	0	1.29E−4	I
CN108-63	G8.2109-0.3777	3.2	6.7	129	1376	0	0	II
CN108-64	G8.2113-0.6432	0.1	4.1	1	249	0	1.80E−4	II
CN108-65	G8.2178-0.6518	0.8	4.5	8	145	0	1.02E−4	II
CN108-66	G8.2188-0.5030	0.3	4.0	2	249	0	1.80E−4	III
CN108-67	G8.2205-0.3947	0.6	5.1	16	509	0	1.27E−3	I
CN108-68	G8.2285-0.6343	0.6	3.9	5	74	0	4.13E−5	II
CN108-69	G8.2352-0.3560	0.9	7.3	7	1942	0	4.67E−4	I
CN108-70	G8.2386-0.3649	0.6	6.2	6	1038	0	4.13E−5	II
CN108-71	G8.2389-0.5381	0.2	10.3	1	1863	0	2.37E−3	I
CN108-72	G8.2399-0.5755	0.5	6.2	7	997	0	3.76E−4	I
CN108-73	G8.2439-0.6591	3.9	4.0	52	53	3.43E−7	3.66E−7	II
CN108-74	G8.2537-0.6294	1.7	3.8	10	157	0	1.88E−5	II
CN108-75	G8.2547-0.3976	2.7	5.7	55	733	0	3.25E−7	II
CN108-76	G8.2568-0.4835	0.1	4.6	1	361	0	1.80E−4	III
CN108-77	G8.2602-0.2906	2.9	5.9	63	843	0	2.07E−7	II
CN108-78	G8.2913-0.6607	0.7	7.3	5	1942	0	2.51E−6	II
CN108-79	G8.2928-0.3444	0.7	4.8	11	383	0	4.99E−4	II
CN108-80	G8.2948-0.6148	1.0	7.3	11	1942	0	4.67E−4	III
CN108-81	G8.2956-0.3215	1.5	5.2	19	499	0	2.40E−4	I
CN108-82	G8.3082-0.3702	1.3	4.7	16	383	0	1.37E−4	III
CN108-83	G8.3127-0.4811	2.6	5.5	32	665	0	1.62E−6	II
CN108-84	G8.3144-0.4821	0.7	8.8	17	1847	0	9.76E−4	I
CN108-85	G8.3217-0.3540	2.4	9.8	186	5808	0	2.63E−3	I
CN108-86	G8.3224-0.4976	17.3	49.6	37170	376600	1.11E−3	4.94E−3	I
CN108-87	G8.3301-0.5619	4.2	7.3	194	1717	0	7.65E−4	I
CN108-88	G8.3357-0.6110	1.2	6.6	33	1324	0	1.33E−3	I
CN108-89	G8.3393-0.3598	3.2	6.4	119	1132	0	2.23E−7	II
CN108-90	G8.3585-0.3805	0.2	7.7	1	548	0	1.59E−3	I
CN108-91	G8.3868-0.4480	0.6	7.7	9	566	0	9.41E−4	I
CS57-1	G353.3612-0.1481	1.0	11.6	110	10020	0	1.62E−3	I
CS57-2	G353.3629-0.1703	6.0	20.0	993	46230	0	4.03E−3	II
CS57-3	G353.3727-0.1019	2.3	11.5	85	5111	0	2.74E−3	II
CS57-4	G353.3833-0.1570	3.7	11.6	152	9883	0	1.75E−3	II

given in Table 1. The projected YSO density is lower inside the 8 μm shell and higher outside the shell to the lower and upper left. There do not appear to be preferred areas of concentrated star formation along the rim, in contrast to CN138. There also appears to be significant star formation beyond the 8 μm PAH emission. This characteristic was observed by Zavagno et al. (2007) in their study of RCW 120. They suggested that an H II region that leaks UV photons ($h\nu > 13.6$ eV) may be carving small-scale tunnels through the PDR, inducing small-scale star formation far from the ionization front. If such a process is occurring around CN108, we do not observe evidence of small-scale radio continuum emission within the PDR, as they did using Hα. It is possible, however, that such a small-scale structure is below the radio-continuum sensitivity limit.

Using the method of Watson et al. (2008), we have identified six sources whose broadband SEDs are consistent with O-type

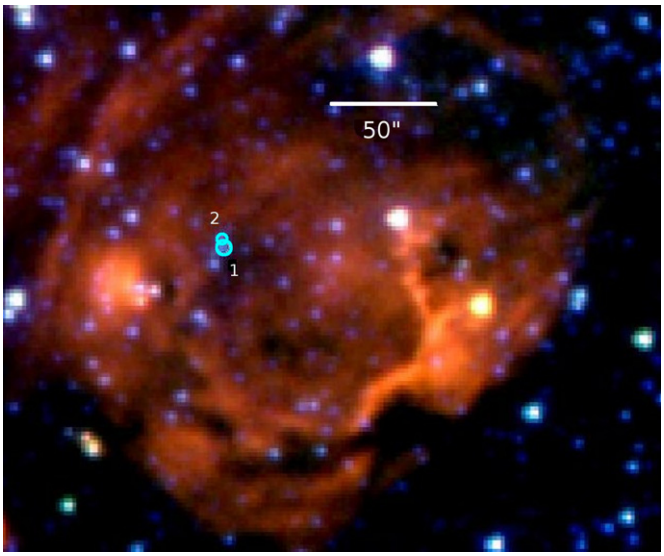

Figure 3. CN138: candidate ionizing stars identified using the method of Watson et al. (2008) overlaid on 8 μm (red), 4.5 μm (green), and 3.6 μm (blue) images. See Table 2 for star properties.

(A color version of this figure is available in the online journal.)

Table 2
Ionizing Star Candidates

ID	Name	Spectral Type
ICN138-1	G9.8420-00.7134	O8.5V
ICN138-2	G9.8421-00.7127	O9.0V
ICN108-1	G8.0903-00.4912	O7.0V
ICN108-2	G8.1090-00.5168	O9.5V
ICN108-3	G8.1375-00.4282	O9.5V
ICN108-4	G8.1541-00.4920	O6.0V
ICN108-5	G8.1565-00.4337	O7.5V
ICN108-6	G8.1566-00.5274	O7.0V

stars at the distance of CN108 (see Table 2 and Figure 6). The sources are grouped in two clumps, one near the center of the upper half of CN108, the other along the 24 μm emission in the lower half of CN108. This split and the 8 μm emission dip toward the center at about $l = 8.^{\circ}18$, $b = -0.^{\circ}48$ imply that there may be two or three sources creating this bubble. Considering that the radio continuum emission implies a single O8 star, however, some of these candidate ionizing stars are likely foreground stars. Unfortunately, without more constraints, we are unable to further isolate the ionizing stars. Because there are likely multiple exciting sources, the shell morphology observed at 24 μm is probably not produced by a wind-blown cavity (as in N49; Watson et al. 2008), but rather hot dust centered on each ionizing star. As further evidence that suggests multiple ionizing sources, the 8 μm emission bubble is scalloped and has multiple centers of curvature. For example, the 8 μm emission at the upper left in Figure 6 curves around source 3 whereas the emission at the lower left curves around source 4.

3.3. CS57

CS57 has a shell morphology at 8 μm surrounding a smaller shell of 24 μm emission (see Figure 7). 20 cm emission was not detected toward the center of CS57 coincident with the 24 μm emission at a surface brightness level $\geqslant$2 mJy beam^{-1} with a beam size of $7'' \times 4''$ (Helfand et al. 2006). 6 cm emission, however, was detected. Several 6 cm (contours in Figure 7)

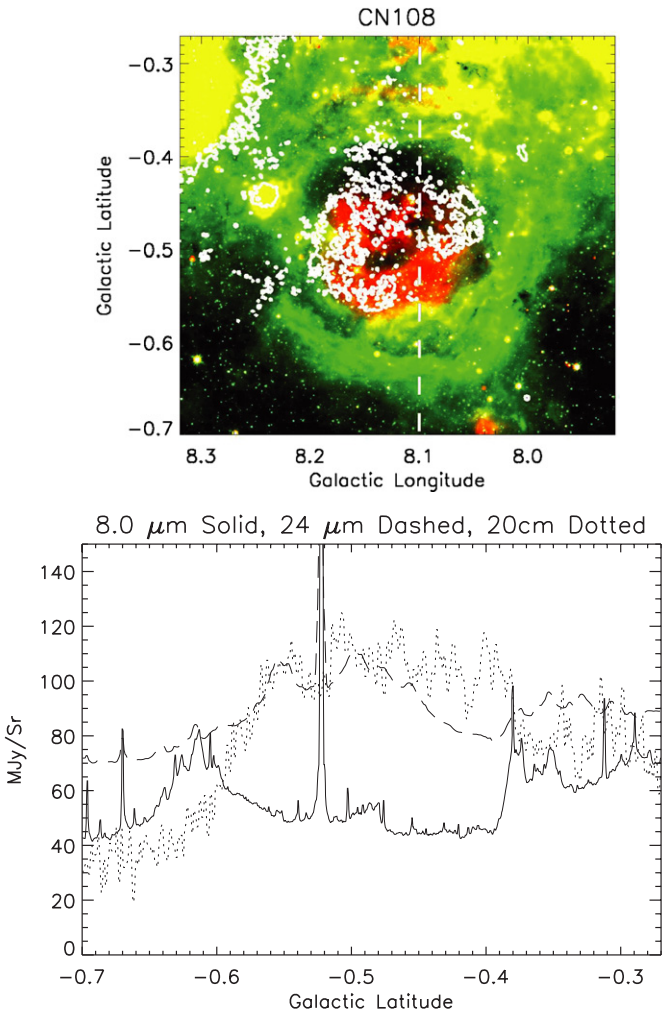

Figure 4. Top: CN108 shown in 24 μm (red), 8 μm (green), and 4.5 μm (blue). 20 cm contoured at 1.1 mJy. Note that the 20 cm is probably over-resolved and thus missing flux. Bottom: the slice is at $l = 8.^{\circ}1$ showing 20 cm (dotted, $\times 10^6$), 24 μm (dashed), and 8.0 μm (solid, $\times 5$). The 24 μm and 20 cm emission is concentrated between the 8 μm peaks that indicate the shell. The 8 μm spike at $b = -0.53$ is caused by a star.

(A color version of this figure is available in the online journal.)

sources are observed along the 8 μm shell and outside the bubble. No radio continuum flux is detected toward the interior of the shell. Its velocity is -58 km s^{-1}, corresponding to a near kinematic distance of 6.2 kpc. We measure an average inner radius at 8 μm of 81″ (4.9 pc) and an average outer radius of 130″ (7.6 pc). Using the inner radius, the near kinematic distance, and the limitation on 20 cm emission, we calculate an upper limit of $N_{\rm Ly} < 3.4 \times 10^{47}$ ionizing photons s^{-1}, equivalent to a star cooler than O9.5V (MSH05). The radius of the 24 μm emission (measured to the brightest intensity ridge) is 45″ (2.7 pc).

The brightest 6 cm radio continuum source (at the bottom of the shell in Figure 7) has an integrated flux density of 350 mJy; 24 μm emission is saturated and pointlike. The small, bright flux at 8 μm ($\sim$10 Jy) and 24 μm (greater than 2 Jy) and $\frac{8\,\mu{\rm m}}{24\,\mu{\rm m}}$ ratio ($\lesssim$5) suggests that this source may be an asymptotic giant branch (AGB) star (see Robitaille et al. 2008), in which case it would likely be unrelated to the bubble. However, the 6 cm emission is consistent with a UCHII region. In such a scenario, the high $\frac{8\,\mu{\rm m}}{24\,\mu{\rm m}}$ ratio could be caused by bright PAH emission in the 8 μm band. Assuming optically thin, free–free emission,

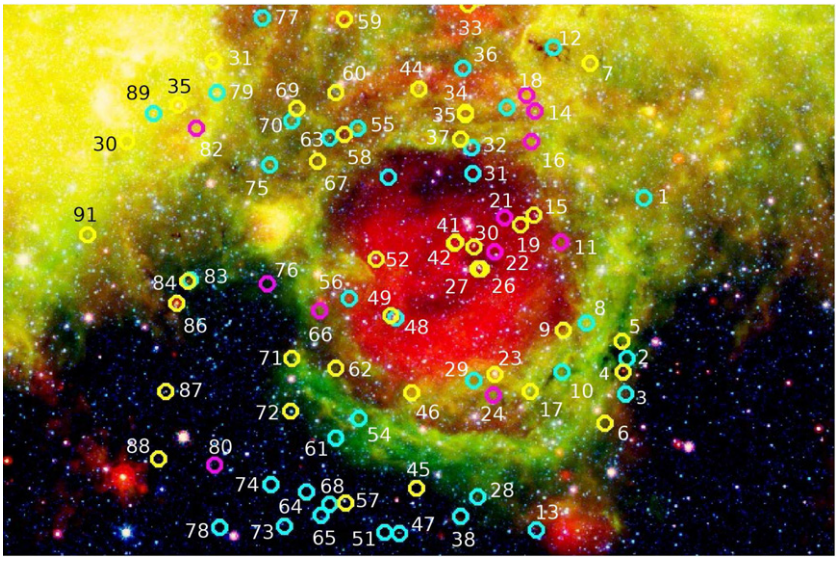

Figure 5. CN108: candidate YSOs overlaid an 24 μm (red), 8.0 μm (green), and 4.5 μm (blue) images. Stage I sources are shown in yellow, stage II in cyan, and stage III in red.

(A color version of this figure is available in the online journal.)

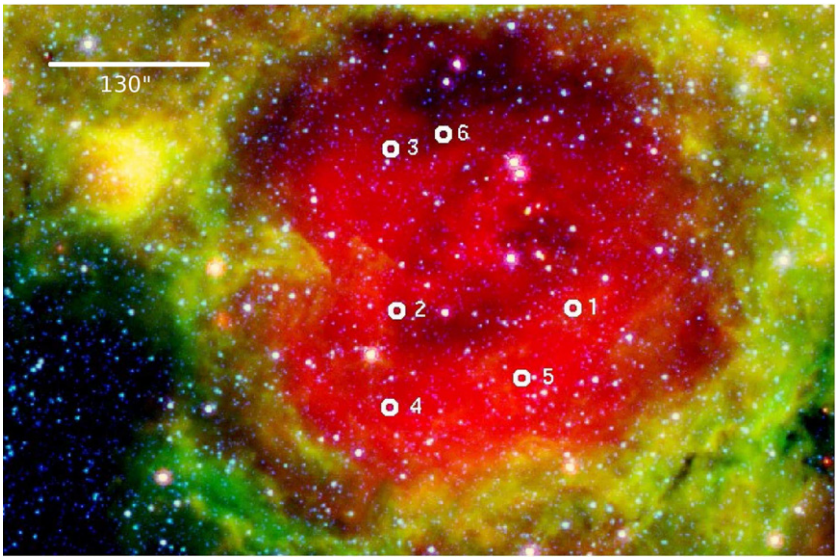

Figure 6. CN108: candidate ionizing stars superimposed on 24 μm (red), 8 μm (green), and 4.5 μm (blue) emission. Not all these sources are ionizing the region, but at least two are likely important, one from 3 and 6 and at least one from 1, 2, 4, and 5.

(A color version of this figure is available in the online journal.)

this flux density implies a UV flux of 9.5×10^{46} photons s^{-1}, equivalent to an early-B star (MSH05). However, massive stars typically form in regions of high star formation of all masses, which we do not observe here. Sugitani et al. (1991) argue that intermediate-mass (1.5–6.0 $M_{\odot}$) star formation may be caused preferentially by triggering. In summary, we cannot definitively classify this source as either an AGB star or massive YSO.

We have identified four sources as probable YSOs associated with CS57 (see Figure 8 for locations and Table 1 for properties). All the YSOs have $M < 10\ M_{\odot}$ and lie either along the 8 μm shell or the 24 μm shell. The low number of YSO candidates is consistent with CS57 representing the low-power end of the bubble population.

We analyzed the GPSC sources to identify the exciting star(s) of CS57. The only two candidates were O6V stars, however. These spectral types are strongly inconsistent with the absence of radio-continuum emission from the bubble center and thus are likely low-mass, foreground stars. Identifying the mid-to-early B star responsible for this bubble is difficult because it is easy to confuse a mid-to-early B star at the bubble's location with a cool, foreground star.

4. ANALYSIS: TRIGGERED STAR FORMATION

We now discuss the likelihood of triggered star formation in each region. Hosokawa & Inutsuka (2006; hereafter HI06) present numerical simulations of expanding H II regions and their associated PDRs. Their models concentrate on incorporating the different physics in the H II region and surrounding swept-up shell. Specifically, they treat the UV- and FUV- radiative transfer and cooling, photo- and collisional ionization, photodissociation, and recombination in the H II region and PDR region (see their Tables 2 and 3 for a summary of the dominant

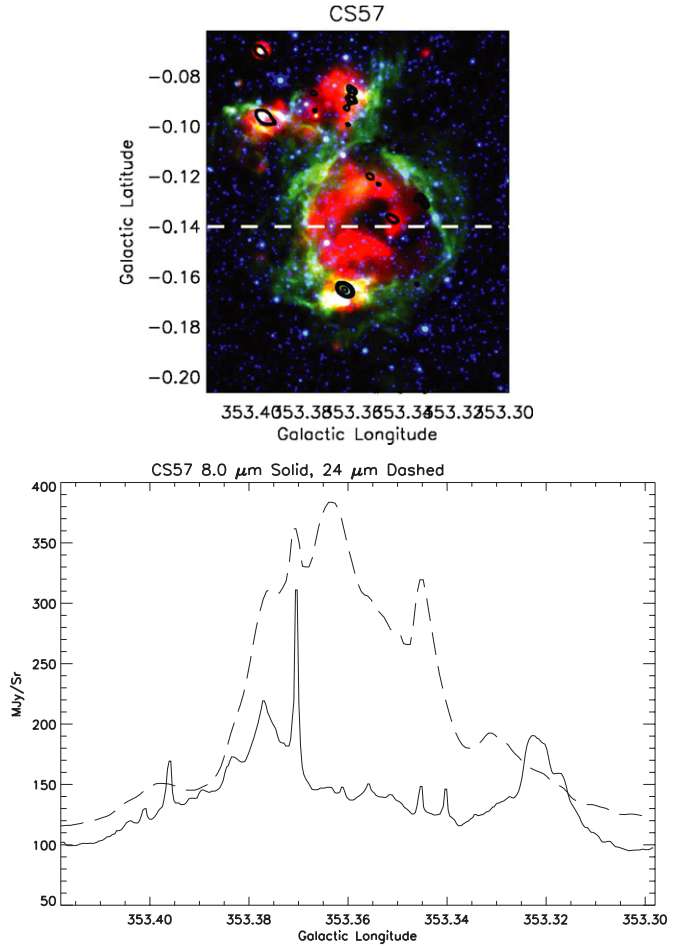

Figure 7. Top: CS57 shown in 24 μm (red), 8 μm (green), and 4.5 μm (blue). 6 cm in contours. No 20 cm emission was detected above 2 mJy beam^{-1}. Note that the 24 μm emission is saturated at the bottom of the shell. Bottom: the slice is at $b = -0.^{\circ}14$ showing 24 μm (dashed), and 8.0 μm (solid, $\times 5$) emission.

(A color version of this figure is available in the online journal.)

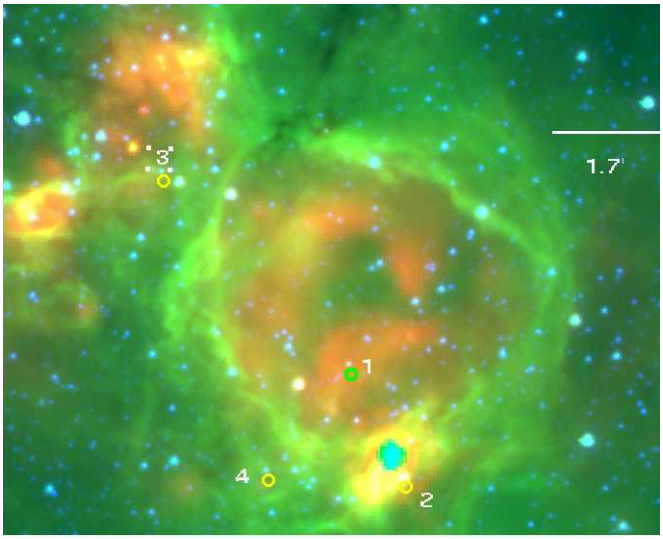

Figure 8. CS57: candidate YSOs superimposed on 24 μm (red), 8 μm (green), and 4.5 μm (blue) emission. Stage I sources are shown in yellow, stage II in cyan, and stage III in green.

(A color version of this figure is available in the online journal.)

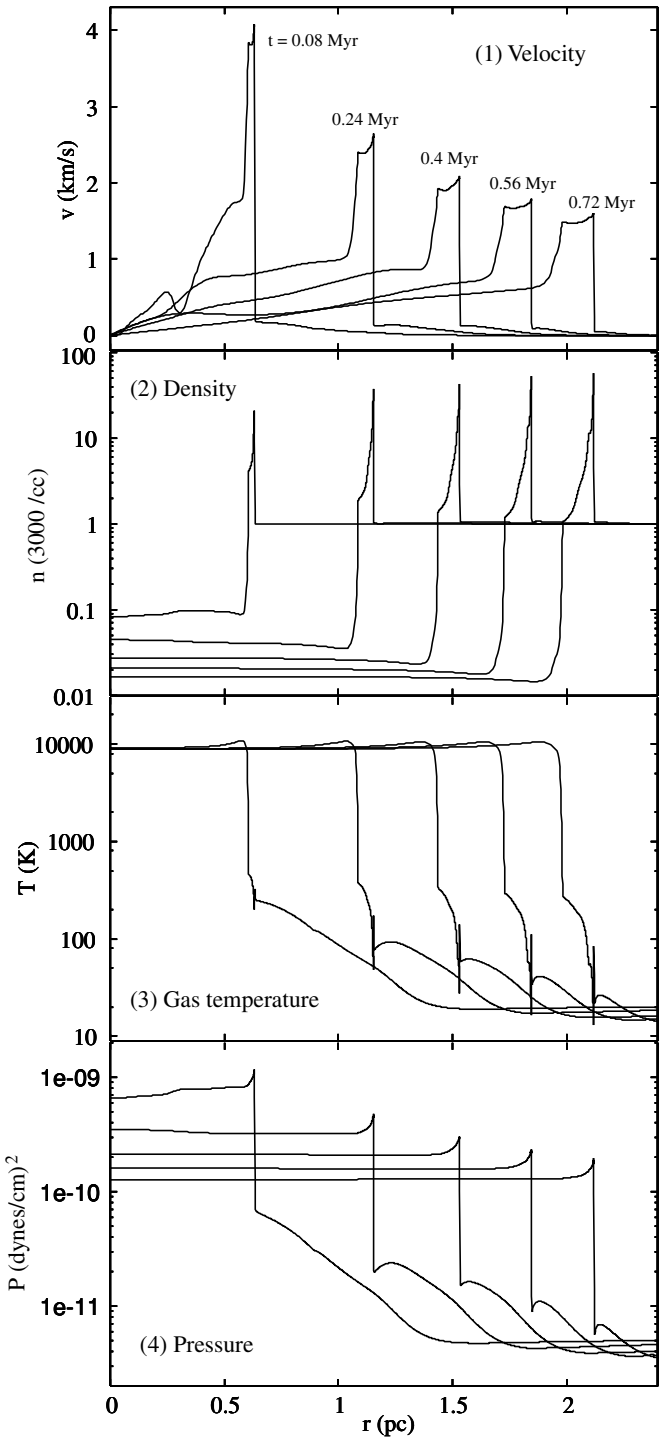

Figure 9. Numerical simulation of the expansion of an H II region, model S19 modified by original authors (T. Hosokawa 2008, private communication) expanding into a dense ISM (3×10^3 cm^{-3}). Model S19 is Figure 11 from Hosokawa & Inutsuka (2006). The ionizing star has a mass $M_* = 19\ M_\odot$. The simulations were one dimensional and incorporated radiative heating and cooling, photo- and collisional ionization, photodissociation, and recombination.

cooling lines in the H II region and PDR). They were principally interested in modeling the progression of the ionization front, dissociation front, and shock front due to an overpressured H II region surrounding a single massive star. Their models do not include stellar winds or cooling in the H II region due to dust emission. We do not expect stellar winds to dominate the late-O and early-B stars we are studying here. Cooling due to dust emission may be important, however, but has not been well studied. HI06 also calculate the time required for swept-up ambient

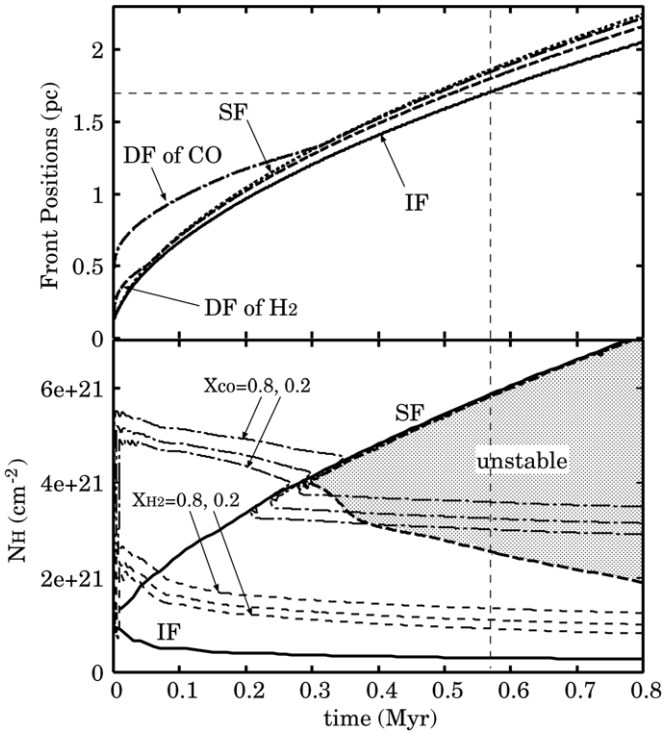

Figure 10. Numerical simulation of an H II region (model S19 modified by T. Hosokawa 2008, private communication) expanding into a dense ISM (3×10^3 cm^{-3}). The dynamics of the original model are shown in Figure 14 from Hosokawa & Inutsuka (2006). The ionizing star has a mass $M_* = 19\ M_\odot$. Top: the position of the shock front (SF), dissociation front (DF), and ionization front (IF) as the H II region expands due to internal overpressure. We use this model to estimate the age of CN138 by matching the observed size of the 8 μm shell (see the dashed line). We also use this model to conclude that the presence of triggered star formation along the shell is consistent with the size of the bubble.

gas to become gravitationally unstable to collapse, possibly resulting in triggered star formation (i.e., the collect-and-collapse mechanism). They present five models of different central stellar masses (11.7 $M_\odot$–101.3 $M_\odot$) and ambient densities (10^2 cm^{-3}–10^4 cm^{-3}). The authors have provided two new models with parameters adjusted so that the observational predictions match the observations presented here. We use a model similar to their model S19, which has a central mass of 19 $M_\odot$. The authors have adjusted the ambient density to 3×10^3 cm^{-3}. The velocity, density, gas temperature, and pressure distributions at different epochs for this model are shown in Figure 9.

If we equate the 8 μm emission inner radius observed here with the position of the H_2 dissociation front, shock front, and ionization front in this model (which are nearly coincident), we can estimate the dynamical age of the bubble. Figure 10 (top panel) shows the growth of these three fronts' radii over time for the modified version of model S19 described above. Based on this assumption, CN138 appears quite young, 0.5–0.6 Myr. HI06 also determine when the shell density would become gravitationally unstable to collapse, implying when triggered star formation could be expected to begin (see Figure 10, bottom panel). In their modified model, gravitational collapse begins at $t = 0.3$ Myr. Thus, we conclude that the size of CN138 is consistent with the presence of triggered star formation. These results, however, are strongly dependent on the assumed ambient density. If we use the published model S19 with an ambient density of 10^3 cm^{-3}, we would conclude that the bubble age is 0.15–0.45 Myr and gravitational collapse begins at $t = 0.5$ Myr, implying that triggered star formation has not started.

Since CN108 appears to involve several bubbles overlapping, its expansion is significantly more complicated than either CN138 or CS57. No model by HI06 includes multiple sources, so we cannot estimate its dynamical age. CS57, on the other hand, is difficult to interpret because we do not know the spectral type of the ionizing star. We use a modified version lowest mass model presented by HI06 (model S12, $M_* = 11\ M_\odot$, $n_{\rm ambient} = 100$ cm^{-3}; T. Hosokawa 2008, private communication). The measured radius (4.9–7.6 pc) is consistent with an age of 3.5–7 Myr. At this stage, T. Hosokawa (2008, private communication) predicts that the shell will be gravitationally unstable. This prediction is consistent with the YSOs we detect along the shell being triggered by the expanding shell.

5. CONCLUSIONS

We have analyzed three late-O/early-B-powered bubbles from the catalog of Churchwell et al. (2007). Our conclusions are as follows.

1. Similar to the higher energy bubbles analyzed previously, each bubble shows the same basic structure, a PDR surrounding hot dust and, in two of the three sources, ionized gas.
2. Potential triggered star formation by the collect-and-collapse mechanism has been identified in two bubbles, CN138 and CS57.
3. Candidate ionizing stars are identified in CN138 and CN108. Based on spectral types implied by their SEDs and radio-continuum emission, the bubbles do not appear to be wind dominated. CN138 appears to be driven by one or two stars that are off-center with spectral types O8.5 and O9. CN108, on the other hand, appears to be driven by two or three hot stars with spectral type between O6 and O9.5.
4. The age of two bubbles are approximated through comparison with modified versions of the numerical models of HI06. The ages of both CS57 and CN138 are consistent with the presence of the identified YSOs being triggered by the bubbles' expansion.

We acknowledge support for this work by NASA contracts 1289406 and 1275394. We also acknowledge the helpful comments of T. Hosokawa, and especially for providing new simulations for comparison with CN138 and CS57.

REFERENCES

Benjamin, R. A., et al. 2003, PASP, 115, 953
Brand, J., & Blitz, L. 1993, A&A, 275, 67
Churchwell, E., et al. 2006, ApJ, 649, 759
Churchwell, E., et al. 2007, ApJ, 670, 428
Deharveng, L., Lefloch, B., Zavagno, A., Caplan, J., Whitworth, A. P., Nadeau, D., & Martín, S. 2003a, A&A, 408, L25
Deharveng, L., Zavagno, A., Salas, L., Porras, A., Caplan, J., & Cruz-González, I. 2003b, A&A, 399, 1135
Elmegreen, B. G. 1998, Origins, 148, 150
Helfand, D. J., Becker, R. H., White, R. L., Fallon, A., & Tuttle, S. 2006, AJ, 131, 2525
Hosokawa, T., & Inutsuka, S. I. 2006, ApJ, 646, 240
Lockman, F. J., Pisano, D. J., & Howard, G. J. 1996, ApJ, 472, 173
Martins, F., Schaerer, D., & Hillier, D. J. 2005, A&A, 436, 1049
Mateen, M., Hofner, P., & Araya, E. 2006, ApJS, 167, 239
Povich, M. S., Benjamin, R. A., Whitney, B. A., Babler, B. L., Indebetouw, R., Meade, M. R., & Churchwell, E. 2008, ApJ, 689, 242
Robitaille, T. P., Whitney, B. A., Indebetouw, R., & Wood, K. 2007, ApJS, 169, 328
Robitaille, T. P., Whitney, B. A., Indebetouw, R., Wood, K., & Denzmore, P. 2006, ApJS, 167, 256
Robitaille, T. P., et al. 2008, AJ, 136, 2413

Scoville, N. Z., Yun, M. S., Sanders, D. B., Clemens, D. P., & Waller, W. H. 1987, ApJS, 63, 821
Shara, M. M., Moffat, A. F. J., Smith, L. F., Niemela, V. S., Potter, M., & Lamontagne, R. 1999, AJ, 118, 390
Slysh, V. I., Val'tts, I. E., Kalenskii, S. V., Voronkov, M. A., Palagi, F., Tofani, G., & Catarzi, M. 1999, A&AS, 134, 115
Sugitani, K., Fukui, Y., & Ogura, K. 1991, ApJS, 77, 59
Walsh, A. J., Hyland, A. R., Robinson, G., & Burton, M. G. 1997, MNRAS, 291, 261
Watson, C., et al. 2008, ApJ, 681, 1341
White, R. L., Becker, R. H., & Helfand, D. J. 2005, AJ, 130, 586
Whitworth, A. P., Bhattal, A. S., Chapman, S. J., Disney, M. J., & Turner, J. A. 1994, MNRAS, 268, 291
Zavagno, A., Deharveng, L., Comerón, F., Brand, J., Massi, F., Caplan, J., & Russeil, D. 2006, A&A, 446, 171
Zavagno, A., Pomarès, M., Deharveng, L., Hosokawa, T., Russeil, D., & Caplan, J. 2007, A&A, 472, 835